Vol. 52 (2021) *Acta Physica Polonica B* No 5

EVOLUTION OF NUCLEAR SHAPES IN LIGHT NUCLEI FROM PROTON- TO NEUTRON-RICH SIDE

Pankaj Kumar[†], Virender Thakur, Smriti Thakur
Vikesh Kumar, Shashi K. Dhiman

Department of Physics, Himachal Pradesh University
Summer-Hill, Shimla-171005, India

(Received February 2, 2021; accepted April 19, 2021)

The relativistic Hartree–Bogoliubov (RHB) model with density-dependent meson-exchange interaction and separable pairing is employed to study the shape evolution and shape coexistence in Mg ($Z = 12$), Si ($Z = 14$), S ($Z = 16$), and Ar ($Z = 18$) isotopes from proton-rich side to neutron-rich side. A sudden shape transition is observed in these isotopic chains. A reasonable agreement of quadrupole deformation is found with the finite range droplet model (FRDM). Our findings of binding energies, quadrupole deformation parameter, charge radii, and isotope shifts are also in good agreement with the results of Hartree–Fock–Bogoliubov calculations based on the D1S-Gogny force. In addition to shape evolution, the disappearance of $N = 28$ shell closure and onset of deformation is also observed towards the neutron-rich side. The modification of $N = 28$ shell gap is related to the quadrupole excitations across it. The present calculations infer the neutron drip line at ^{40}Mg.

DOI:10.5506/APhysPolB.52.401

1. Intoduction

The study of nuclei far from the β-stability line (exotic nuclei) is a devoted part of modern nuclear-structure studies. The limit of nuclear existence is reached while going away from the stability line. Nuclear drip lines form the edges of the nuclear chart and are defined as limits beyond which a single nucleon becomes unbound in the nuclear ground state. The advancement in Radioactive Ion Beam (RIB) facilities and sensitive detection technologies has made it accessible to study the structure and properties of these nuclei.

[†] Corresponding author: `pankajdhiman659@gmail.com`

The evolution of ground-state shape from proton-rich side to neutron-rich side is a frontier area in nuclear physics. The shape evolution in isotonic or isotopic chains has been investigated consistently by various theoretical and experimental techniques. The results obtained from the electron and in-beam spectroscopy experiment reveal the prolate-spherical shape coexistence for ^{44}S, with intruder configuration being the ground state [1, 2]. This intruder ground state was predicted to be due to the quadrupole excitation across the $Z = 14$ and $N = 28$ shell gaps. An exhaustive study of the evolution of shapes and other ground-state properties in light nuclei is done in Ref. [3]. They have employed relativistic mean-field (RMF) theory with NL-SH force and with BCS pairing in the calculations. The nuclear deformation in light even–even isotopes has been investigated with the Hartree–Fock–Bogoliubov (HFB) model using SLy4 Skyrme parameterization [4]. The relation between single-particle motion and potential energy surfaces has been studied by taking deformation into account. The large-amplitude collective dynamics of shape phase transition in the low-lying states of $^{30-36}$Mg and shape coexistence in excited 0^+ state in ^{32}Mg has been investigated in Refs. [5, 6], respectively. The study of shape evolution for $^{28-42}$Si isotopes has been done within the framework of the Skyrme–Hartree–Fock model by employing BCS approximation for the pairing channel [7]. Shape coexistence and triaxial deformation in Ne, Na, Mg, and Al isotopes have also been studied by Davies *et al.* [8]. One of the prominent subjects in the study of nuclear structure of exotic nuclei, in the light region, is the evanescence of the traditional magic numbers and the emergence of new ones. The weakening of the $N = 28$ shell closure and the development of deformation has been observed in low-energy Coulomb excitation experiments [9–11]. Their study indicated a prolate shape of the ^{44}Ar nucleus by calculating $B(\mathrm{E2})$ values and the spectroscopic quadrupole moment of the 2_1^+ state from the differential Coulomb excitation cross sections. Many theoretical studies have been done on the shape evolution in $N = 28$ isotones and reduction of shell gaps [12–15].

The nuclear density functional theories have been used to understand nuclear many-body dynamics for an appreciable description of nuclei near the drip lines [16–22]. The RHB model has been employed to study shell structure of Si, S, Ar, and Ca isotopes in recent papers [18–20]. In these papers, binding energies and their derivative properties have been studied by taking considering spherical symmetry. Their results indicate the presence of $N = 14$ sub-shell closure and also reproduce the traditional magic numbers ($N = 8$, 20, and 28). However, to throw some light on the effect of deformation on light nuclei from proton to neutron-rich side, we have performed quadrupole constrained RHB calculations using density-dependent meson exchange (DD-ME2) parameter set [23] with pairing interaction which is separable in momentum space. An extensive study of shape evolution and shape coexistence is done for Mg, Si, S, and Ar even–even isotopes. The other ground-state observables are also studied. The present calculations do not provide any indication about $N = 14$ sub-shell closure in these isotopes rather, the disappearance of $N = 28$ shell closure is observed. In the present manuscript, we have briefly presented the impact of deformation on the shell structure of even–even Mg, Si, S, and Ar isotopes.

The organization of this paper is as follows: A brief description of the RHB model with meson-exchange coupling and with separable pairing is presented in Section 2. Results and discussion for shape evolution and various ground-state observables, compared with experimental data, are presented in Section 3. Finally, the concluding remarks of the present analysis are given in Section 4.

2. Theoretical framework

Self-consistent mean-field (SCMF) models provide a very successful tool to study nuclear ground-state properties and excited-state properties from the valley of β-stability to the nuclear drip lines throughout the entire nuclear chart. These models are based on the nuclear energy density functionals (EDF) in which the nucleons are treated as independent particles moving inside the nucleus under the influence of potentials that are derived from such functionals [24]. In the relativistic case, the nucleons are treated as Dirac spinors that interact by the exchange of virtual mesons, as described by Refs. [25–29].

2.1. Lagrangian density for the meson exchange models

The total Lagrangian density of mesons exchange model can be written as [23, 30]

$$\begin{aligned}\mathcal{L} = & \sum_i \bar{\psi}_i (i\gamma_\mu \partial^\mu - m)\psi_i + \tfrac{1}{2}\partial_\mu \sigma \partial^\mu \sigma - \tfrac{1}{2} m_\sigma^2 \sigma^2 - \tfrac{1}{2}\Omega_{\mu\nu}\Omega^{\mu\nu} \\ & + \tfrac{1}{2} m_\omega^2 \omega_\mu \omega^\mu - \tfrac{1}{4}\vec{\boldsymbol{R}}_{\mu\nu}\vec{\boldsymbol{R}}^{\mu\nu} + \tfrac{1}{2} m_\rho^2 \vec{\rho}_\mu \cdot \vec{\rho}^{\,\mu} - \tfrac{1}{4}\boldsymbol{F}_{\mu\nu}\boldsymbol{F}^{\mu\nu} \\ & - g_\sigma \bar{\psi}\psi\sigma - g_\omega \bar{\psi}\gamma^\mu \psi \omega_\mu - g_\rho \bar{\psi}\vec{\tau}\gamma^\mu \psi \cdot \vec{\rho}_\mu - e\bar{\psi}\gamma^\mu \psi A_\mu \,, \end{aligned} \tag{1}$$

where m denotes the bare mass of nucleon and ψ denotes the Dirac spinors. m_σ, m_ω, m_ρ are masses of σ, ω, ρ mesons with corresponding coupling constants g_σ, g_ω, g_ρ for the mesons to the nucleons, respectively. $\Omega_{\mu\nu}$, $\vec{R}_{\mu\nu}$, $F_{\mu\nu}$ are field tensor of the vector fields ω, ρ, and the photon. Arrows denote isovectors and boldface symbols are used for vectors in ordinary space.

From the Lagrangian density in Eq.(1), one can obtain the Hamiltonian density $\mathcal{H}(\boldsymbol{r})$ and hence obtain the total energy which depends on the Dirac spinors and the meson fields by integrating the Hamiltonian density over the r-space [31]

$$\begin{aligned}
&\mathcal{E}_{\mathrm{RMF}}\left[\psi,\bar{\psi},\sigma,\omega^{\mu},\vec{\rho}^{\,\mu},A_{\mu}\right] = \int \mathrm{d}^3r\mathcal{H}(\boldsymbol{r}) = \sum_{i=1}^{A}\int \mathrm{d}^3r\psi_i^{\dagger}(\boldsymbol{\alpha p}+\beta m)\psi_i \\
&+\frac{1}{2}\int \mathrm{d}^3r\left((\nabla\sigma)^2+m_{\sigma}^2\sigma^2\right)-\frac{1}{2}\int \mathrm{d}^3r\left((\nabla\omega)^2+m_{\omega}^2\omega^2\right) \\
&-\frac{1}{2}\int \mathrm{d}^3r\left((\nabla\rho)^2+m_{\rho}^2\rho^2\right)-\frac{1}{2}\int \mathrm{d}^3r(\nabla A)^2 \\
&+\int \mathrm{d}^3r\left(g_{\sigma}\rho_s\sigma+g_{\omega}j_{\mu}\omega^{\mu}+g_{\rho}\vec{j}_{\mu}\cdot\vec{\rho}^{\,\mu}+ej_{p\mu}A^{\mu}\right). \qquad (2)
\end{aligned}$$

The single-nucleon Dirac equation is derived by variation of the energy density functional (2) with respect to $\bar{\psi}$ and takes a simple form that includes only the vector potential $V(\boldsymbol{r})$ and the effective mass $M^*(\boldsymbol{r})=m+g_{\sigma}\sigma$

$$\{-i\boldsymbol{\alpha}\nabla+\beta M^*(\boldsymbol{r})+V(\boldsymbol{r})\}\psi_i(\boldsymbol{r}) \;=\; \epsilon_i\psi_i(\boldsymbol{r})\,. \qquad (3)$$

The vector potential reads

$$V(\boldsymbol{r})=g_{\omega}\omega+g_{\rho}\tau_3\rho+eA_0+\Sigma_0^{\mathrm{R}}\,, \qquad (4)$$

where Σ_0^{R} denotes the rearrangement term arising from the density dependence of the vertex functions (g_{σ}, g_{ω} and g_{ρ}) and is defined as

$$\Sigma_0^{\mathrm{R}}=\frac{\partial g_{\sigma}}{\partial\rho_v}\rho_s\sigma+\frac{\partial g_{\omega}}{\partial\rho_v}\rho_v\omega+\frac{\partial g_{\rho}}{\partial\rho_v}\rho_{tv}\rho\,. \qquad (5)$$

ρ_{tv} denotes the isovector density which is the difference between the proton and the neutron vector density. The functionals are described by density-dependent coupling constants $g_i(\rho)$ (for $i=\sigma,\omega,\rho,\delta$). The coupling of σ field and ω field to the nucleon field is given by [32–34]

$$g_i(\rho)=g_i(\rho_{\mathrm{sat}})f_i(x) \quad \text{for} \quad i=\sigma,\omega \qquad (6)$$

with

$$f_i(x)=a_i\frac{1+b_i(x+d_i)^2}{1+c_i(x+d_i)^2} \qquad (7)$$

which is a function of $x=\rho/\rho_{\mathrm{sat}}$. Here, ρ_{sat} ($=0.152$ fm^{-3}) is the baryon density at saturation in symmetric nuclear matter.

For density dependence of ρ-meson coupling, Dirac–Brueckner suggested the functional form [35], given by

$$g_{\rho}(\rho)=g_{\rho}(\rho_{\mathrm{sat}})\mathrm{e}^{-a_{\rho}(x-1)}\,. \qquad (8)$$

The isovector channel is parameterized by $g_{\rho}(\rho)$ and a_{ρ}.

2.2. Relativistic Hartree–Bogoliubov approximation with a separable pairing interaction

The incorporation of pairing correlations is important to understand the structure phenomena in open shell nuclei quantitatively [36, 37]. The formulation of RHB model is found to be a relativistic extension of the HFB model in which mean-field and pairing correlations are treated self-consistently. The RHB model provides a unified description of particle–hole (ph) and particle–particle (pp) correlations on a mean-field level by using the average self-consistent mean-field potential that encloses the long-range ph correlations and a pairing field potential which sums up the pp correlations. In the RHB model, density matrix in the presence of pairing can be generalized in two densities, the normal density $\hat{\rho}$, and pairing tensor $\hat{\kappa}$. The relativistic Hartree–Bogoliubov energy density functional can be written as

$$E_{\mathrm{RHB}}[\hat{\rho}, \hat{\kappa}] = E_{\mathrm{RMF}}[\hat{\rho}] + E_{\mathrm{pair}}[\hat{\kappa}] \,, \tag{9}$$

where $E_{\mathrm{RMF}}[\hat{\rho}]$ is the nuclear energy density functional and is given in Eq. (2). The pairing part of RHB functional is given by

$$E_{\mathrm{pair}}[\hat{\kappa}] = \frac{1}{4} \sum_{n_1 n_1'} \sum_{n_2 n_2'} \kappa^*_{n_1 n_1'} \left\langle n_1 n_1' \middle| V^{\mathrm{PP}} \middle| n_2 n_2' \right\rangle \kappa_{n_2 n_2'} \,, \tag{10}$$

where $\left\langle n_1 n_1' | V^{\mathrm{PP}} | n_2 n_2' \right\rangle$ are the matrix elements of the two-body pairing interaction, and indices n_1, n_1', n_2, and n_2' denote quantum numbers that specify the Dirac indices of the spinor. The quasiparticle wave functions U_k and V_k are obtained by the variational principle from the solution of relativistic Hatree–Bogoliubov equations. In coordinate representation

$$\begin{pmatrix} h_{\mathrm{D}} - m - \lambda & \varDelta \\ -\varDelta^* & -h_{\mathrm{D}}^* + m + \lambda \end{pmatrix} \begin{pmatrix} U_k(r) \\ V_k(r) \end{pmatrix} = E_k \begin{pmatrix} U_k(r) \\ V_k(r) \end{pmatrix} . \tag{11}$$

In the self-consistent relativistic mean-field calculation, $\hat{h}_{\mathrm{D}}$ is the single-nucleon Dirac Hamiltonian and m is the mass of nucleon. The λ chemical potential is determined by the particle number subsidiary condition such that the expectation value of the particle number operator in the ground state equals the number of nucleons. The pairing field $\varDelta$ reads

$$\varDelta_{n_1 n_1'} = \frac{1}{2} \sum_{n_1 n_2'} \left\langle n_1 n_1' \middle| V^{\mathrm{PP}} \middle| n_2 n_2' \right\rangle \kappa_{n_2 n_2'} . \tag{12}$$

The pairing force is separable in momentum space and in r-space has the form of

$$V^{\mathrm{PP}} \left(\boldsymbol{r_1}, \boldsymbol{r_2}, \boldsymbol{r_1'}, \boldsymbol{r_2'} \right) = -G \delta \left(\boldsymbol{R} - \boldsymbol{R'} \right) P \left(\boldsymbol{r} \right) P(\boldsymbol{r'}) \,, \tag{13}$$

where $\boldsymbol{R} = \frac{1}{\sqrt{2}}(\boldsymbol{r_1} + \boldsymbol{r_2})$ and $\boldsymbol{r} = \frac{1}{\sqrt{2}}(\boldsymbol{r_1} - \boldsymbol{r_2})$ represent the center of mass and the relative coordinates, respectively, and the form factor $P(\boldsymbol{r})$ is of the Gaussian form written as

$$P(\boldsymbol{r}) = \frac{1}{(4\pi a^2)^{3/2}} \mathrm{e}^{-r^2/2a^2} \,. \tag{14}$$

The two parameters G and a have been adjusted to reproduce the density dependence of gap at the Fermi surface. The values of these parameters in the present work are taken as $G = 728$ MeV fm^3 and $a = 0.644$ fm for protons and neutrons. It is derived in Refs. [36, 38–40] calculated with the DIS Gogny force. The pairing force has a finite range and also it conserves translational invariance due to the presence of the factor $\delta(\boldsymbol{R} - \boldsymbol{R'})$. Even though this force is not completely separable in coordinate space, however, the anti-symmetrized pp matrix elements can be represented as a sum of a finite number of separable terms in the harmonic oscillator basis

$$\left\langle n_1 n_2 \left| V^{\mathrm{PP}} \right| n_1' n_2' \right\rangle_a = \sum_N W^{N*}_{n_1 n_2} W^{N}_{n_1' n_2'} \,. \tag{15}$$

The pairing field $\varDelta$, in this case, takes the form

$$\varDelta_{n_1 n_2} = \sum_N P_N W^{N*}_{n_1 n_2} \quad \text{with} \quad P_N = \frac{1}{2} \mathrm{Tr}\left(W^N \kappa\right) \,, \tag{16}$$

and finally, the pairing energy in the nuclear ground state is given by

$$E_{\mathrm{pair}} = -G \sum_N P_N^* P_N \,. \tag{17}$$

The total energy E_{tot} [MeV] for the nuclear system with A (mass number) nucleons can be calculated as [41]

$$E_{\mathrm{tot}} = E_{\mathrm{RMF}} + E_{\mathrm{pair}} + E_{\mathrm{cm}} \,. \tag{18}$$

Here, E_{cm} accounts for the center-of-mass correction and is given as $E_{\mathrm{cm}} = -\frac{\langle \boldsymbol{P}^2 \rangle}{2Am}$, where $\langle \boldsymbol{P} \rangle = \sum_i^A \boldsymbol{p_i}$ is the total momentum of the nucleus in the center-of-mass frame with A nucleons [42].

2.3. Details of calculations

The pairing correlations play an important role in the understanding of ground-state properties of the open-shell nuclei. Pairing has been included in the relativistic Hartree–Bogoliubov model in the form of simple constant gap approximation, where the pairing gap $\varDelta$ is obtained from odd–even mass differences. The input parameters required to carry out explicit numerical calculations are [26]: *(i)* the baryon and meson masses m, m_σ, m_ω, and m_ρ; *(ii)* the coupling constants of the meson fields to the nucleons g_σ, g_ω, and g_ρ; *(iii)* the number of oscillator shells for fermions and bosons (N_F and N_B); *(iv)* the basis parameters used for the expansion of the Dirac spinor and the meson fields. The meson masses and the coupling constants, calculated using χ^2 fitting procedure, for the DD-ME2 interaction are

$$\begin{aligned} M &= 939\ \text{MeV}\,, \qquad m_\sigma = 550.1238\ \text{MeV}\,, \qquad m_\omega = 783\ \text{MeV}\,,\\ m_\rho &= 763\ \text{MeV}\,, \qquad g_\sigma = 10.5396\,, \qquad g_\omega = 13.0189\,,\\ g_\rho &= 3.6836\,. \end{aligned}$$

For the calculations of the shape evolution and ground-state properties, we have used the DIRHBZ numerical code developed by Nikšić *et al.* [31].

In the mean-field formalism, the maximum number of harmonic oscillator shells in the expansion of fermion and boson fields have to be used to achieve a reliable convergence. However, the computation time increases dramatically with the increase in number of shells. This problem can be tackled by limiting the number of shells, that can be done by studying the convergence behavior. In the present work, we have chosen $N = 28$ isotones of Mg, Si, S, and Ar to obtain the reliable values of binding energy per nucleon, charge radius ($R_{\rm ch}$), and quadrupole deformation parameter (β_2) by performing calculations with the number of oscillator shells ranging from $N_F = N_B = 12$–20. Figure 1 presents the results of total binding energy, binding energy per nucleon (E/A), charge radius ($R_{\rm ch}$), and quadrupole deformation parameter, β_2 (*optimized for each constrained value of deformation parameter*) as a function of the number of oscillator shells ($\boldsymbol{N}$). The variation of binding energy with an increase in number of oscillator shells is 0.12% for ^{40}Mg while, this variation is around 0.03% for $N = 28$ isotones of Si, S, and Ar. The increase of $N_F = N_B$ from 12 to 20 changes the E/A by about 0.12–0.03% and $R_{\rm ch}$ by 0.14–0.06%, while quadrupole deformation parameter β_2 by 2–4% for these isotones of $N = 28$. Therefore, to save computation time and to obtain reasonably converging mean-field solutions, 12 major oscillator shells are adopted in the present study.

In principle, the harmonic oscillator (HO) basis has served as an extremely useful tool in the nuclear structure study. However, for weakly bound systems with large spatial extension, it does not work due to its localization [43]. One has to use extremely large major oscillator shells to reproduce the density of a weakly bound nucleus, which is not feasible in practice (see Figs. 1 and 2 in Ref. [43]). The RHB equations are solved in coordinate space for the description of halo nuclei [44–46]. Later on, it was

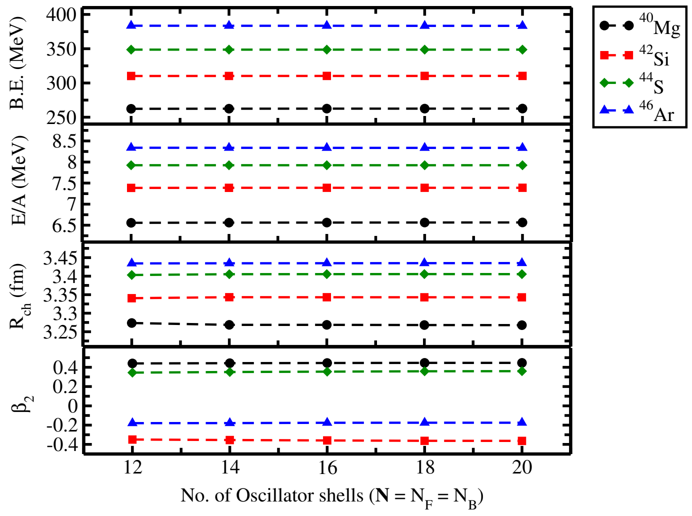

Fig. 1. The results of convergence study of the total binding energy, binding energy per nucleon, charge radii (R_{ch}), and quadrupole deformation parameter (β_2) for $N=28$ isotone of Mg, Si, S, and Ar nuclei as a function of oscillator shells ($\boldsymbol{N}=N_F=N_B$).

observed that the solution of RHB equations in Woods–Saxon (WS) basis provides a successful description of drip-line nuclei [47–50] where the radial wave function has a proper asymptotic behavior at a large distance from the center. Therefore, the WS basis is recommended over the HO basis for solving RHB equations in weakly bound systems.

3. Results and discussion

3.1. Quadrupole deformation and shape coexistence

The main purpose of the present work is to study the deformation systematics in light nuclei from proton-rich side to neutron-rich side. We have performed axially constrained RHB calculations using DD-ME2 parameter set for the entire isotopic chain of Mg, Si, S and Ar to obtained the variation of binding energies with respect to quadrupole deformation parameter β_2. In mean-field approximations, the quadrupole deformation parameter β_2 is related to intrinsic quadrupole moment Q_{20} and is defined as

$$\beta_2 = \sqrt{\frac{5\pi}{9}}\frac{Q_{20}}{AR_0^2}\,, \tag{19}$$

with $R_0 = 1.2A^{1/3}$. The resulting plots of total energy *versus* quadrupole deformation are called potential energy curves (PECs). The analysis of shape evolution starts with a self-consistent relativistic Hartree–Bogoliubov (RHB) calculation of quadrupole binding energy curves. It has been studied in Ref. [50] that at the local minimum in the PEC, the constrained and the unconstrained solutions are identical. One would have the same ground state with the self-consistent unconstrained calculations. Sometimes, however, the constrained calculations are also necessary for a soft PEC, or if many local minima are close to each other. We have used a small step of deformation in the present calculations to obtain the ground state of various nuclei. Due to this small deformation step, the ground state can be found to be very close to the real ones obtained by unconstrained calculations.

Figures 2–5 show the potential energy curves (PECs) for even–even isotopes of Mg, Si, S, and Ar, respectively. The energies are normalized with respect to the total energy of the absolute minima. Figure 2 presents the PECs for Mg isotopic chain which starts from $N = 8$ shell closure. The deformed shapes are seen to evolve between the shell closures. In Fig. 2, the potential energy curve for ^{20}Mg has a spherical shape which is expected for magic neutron number $N = 8$. A sudden shape transition from spherical to prolate is observed as one moves from ^{20}Mg to ^{22}Mg. A large prolate deformation minimum ($\beta_2 = 0.5$) is seen for ^{22,24}Mg nuclei. The shape becomes oblate for ^{26}Mg and a spherical shape is restored for ^{32}Mg due to $N = 20$ shell closure. On moving towards the more neutron-rich side, a prolate min-

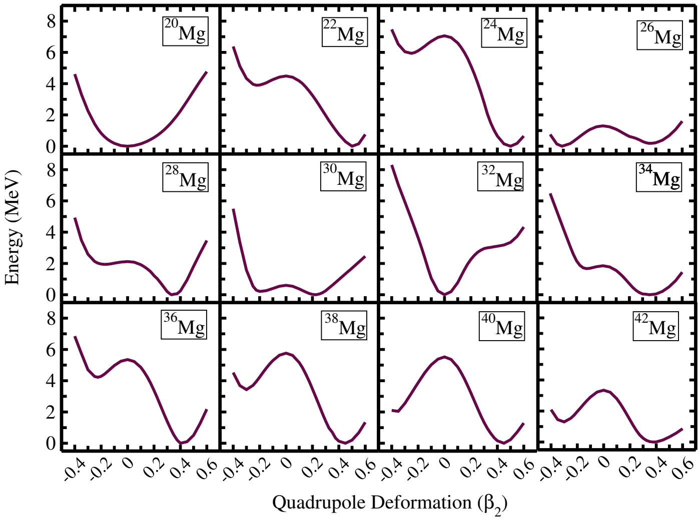

Fig. 2. The potential energy curves (PECs), calculated using the RHB model, as a function of the quadrupole deformation parameter, β_2, for Mg isotopes. For each nuclei, the energies are normalized with respect to the binding energy of the absolute minima.

imum is seen for $^{34-40}$Mg isotopes with quadrupole deformation between $\beta_2 \approx 0.35$–0.45. An oblate–prolate shape coexistence is also observed for ^{26}Mg and ^{30}Mg isotopes.

The PECs for the even–even isotopes of Si are shown in Fig. 3. It can be observed that most of the Si isotopes favor an oblate shape minimum on moving away from $N = 8$ shell closure. ^{26}Si have a ground-state prolate minimum with quadrupole deformation $\beta_2 = 0.40$ coexisting with an almost degenerate oblate minima with $\beta_2 = 0.30$. In addition to this, the isotopes ^{24}Si, ^{26}Si, ^{30}Si, ^{38}Si and ^{40}Si show the phenomena of shape coexistence. The study of shape evolution for S isotopic chain starts from ^{26}S ($Z = 16$, $N = 10$) which exhibits very small prolate deformation. A sudden rise in the quadrupole deformation parameter is observed on moving from ^{26}S to ^{28}S, see Fig. 4. It is interesting to observe a staggering behavior of β_2 on moving towards $N = 20$ shell closure. The sign of the deformation parameter changes in each step with an increase in neutron number. A spherical shape is observed for ^{36}S as expected due to the magic neutron number, $N = 20$. The potential energy curves show a prolate ground-state minimum from $^{38-46}$S isotopes. The shape again becomes oblate for $^{48-52}$S isotopes. It is worth to note that the ground state the minimum for ^{56}S is spherical in the potential energy curve supporting the presence of $N = 40$ sub-shell closure. In addition to these shape transitions, an oblate–prolate shape coexistence is also seen for many sulfur isotopes. Figure 5 presents the PECs for Ar isotopic chain. The chain of isotopic study starts from $Z = 10$

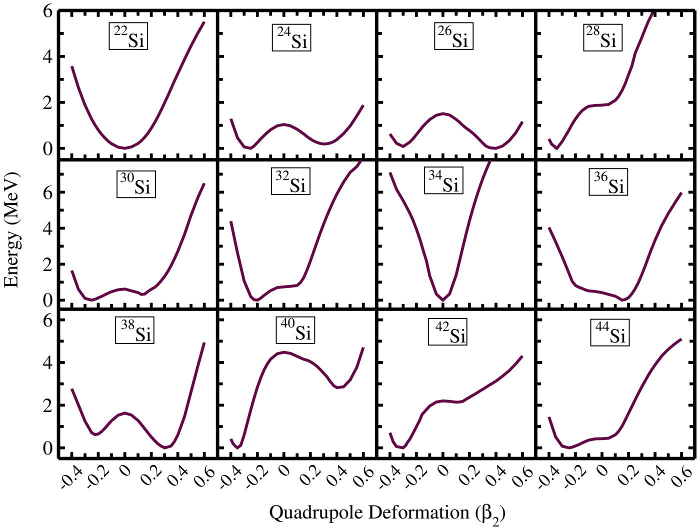

Fig. 3. The same as described in the caption of Fig. 2 but for Si isotopes.

and terminates at $N = 40$. It can be observed from the figure that most of the Ar isotopes are oblate in their ground state. A spherical ground-state shape is observed for nuclei with neutron numbers $N = 20$ and $N = 40$.

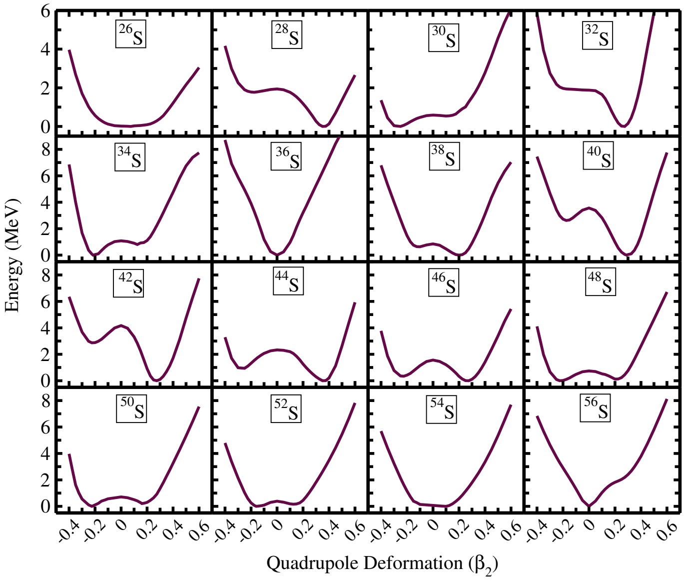

Fig. 4. The same as described in the caption of Fig. 2 but for S isotopes.

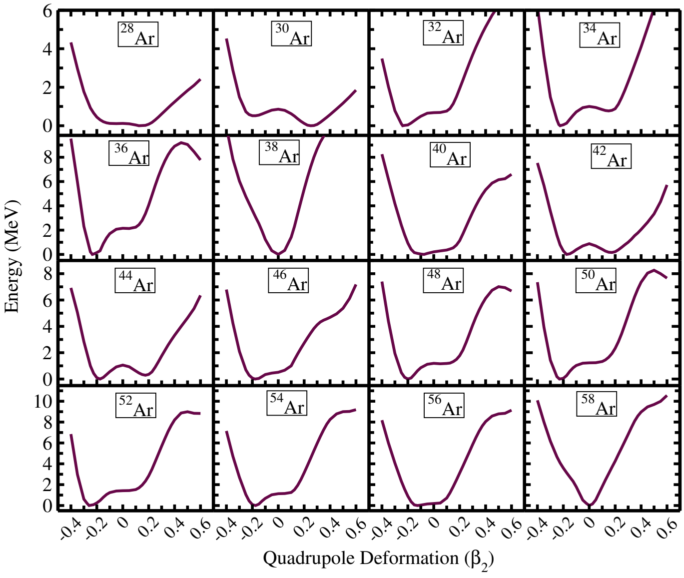

Fig. 5. The same as described in the caption of Fig. 2 but for Ar isotopes.

It should be noted that some of the shape coexisting nuclei with axial deformation might correspond to a triaxial ground state. However, to investigate it, one has to consider the triaxial degree of freedom in the calculations. The RMF approach with triaxiality was firstly developed by Koepf and Ring [51]. The beyond-RMF study done by Yao *et al.* [52] found the triaxial ground state for ^{26}Mg. In the Gogny-HFB calculations, a considerable triaxial ground-state deformation is observed for ^{24}Si and ^{44}Ar [53]. A recent study of light nuclei by Wang *et al.* [54] found a triaxial ground state in shape-coexisting nuclei ^{38}Si, ^{46}S and ^{48}S. However, their results indicate that the triaxiality effect on the mean-field part of nuclear binding energy in these nuclei is marginal.

In Figs. 2–5, the disappearance of $N = 28$ shell closure is also observed. The $N = 28$ isotones, ^{40}Mg, ^{42}Si, ^{44}S, and ^{46}Ar, have some finite deformations indicating the disappearance of $N = 28$ shell closure. An interesting case of study is seen for ^{44}S (an isotone of $N = 28$) which shows an oblate–prolate shape coexistence. This observation is in agreement with the experimental observation [55, 56] and with the predictions of various theoretical results [12–14].

The overall calculated results of binding energies, quadrupole deformation parameter, and charge radii for even–even isotopes of Mg, Si, S, and Ar nuclei are summarized in Tables I–IV. These results are calculated using axially constrained RHB calculations with pairing force which is separable in momentum space. The findings of nuclear observables with DD-ME2 interaction are compared with the results of the HFB model with D1S-Gogny interaction [53] and with the available experimental data [57–60]. The use of different interactions between the nucleons leads to the variation in the ground-state shapes in the two models. The study of nuclear drip lines is itself a very broad and interesting area. Different theoretical models have remarkably divergent predictions about neutron drip lines [61]. Considering the case of Mg isotopes, different neutron drip line predictions have been proposed. According to the study done in Ref. [62], the heaviest magnesium isotope observed is ^{40}Mg, while the drip line is found at ^{42}Mg in some recent studies [63, 64]. A recent study done using the deformed RHB theory in continuum predicts ^{46}Mg as a drip-line nucleus [65]. In our present study, the neutron drip line in Mg isotopic chain is predicted for the ^{40}Mg nucleus subjected to a negative value of two-neutron separation energy ($S_{2n}(Z,N) = E_{\mathrm{b}}(Z,N) - E_{\mathrm{b}}(Z,N-2)$) for ^{42}Mg. In terms of the chemical potential (λ_n), the separation energy can be written as $S_{2n} \approx -2\lambda_n$ [61]. A positive value of λ_n ($= 0.6293$) for ^{42}Mg results in the negative value of S_{2n}, leading to an unbound system. On the proton-rich side, the stability of a nuclei can be investigated by calculating two-proton separation energy ($S_{2p}(Z,N) = E_{\mathrm{b}}(Z,N) - E_{\mathrm{b}}(Z-2,N)$). The negative values of S_{2p}

for ^{22}Si,^{26}S, ^{28}Ar and for ^{30}Ar nuclei indicate these systems to be unstable/unbound to the proton emission. Nuclei with small values of S_{2n} and S_{2p} exhibit the characteristics of a somewhat loosely bound system. It can be observed that the neutron-rich nuclei ^{56}S, in the sulfur isotopic chain, have a very low value of two-neutron separation energy (S_{2n}) leading to an unbound system.

TABLE I

The binding energy (in MeV), the quadrupole deformation parameter β_2, and root-mean-square charge radii R_{ch} for the ground states and a few intrinsic excited states of $^{20-42}$Mg isotopes compared with that of D1S-Gogny [53] and with available experimental data [57–60].

Nuclei	DD-ME2			D1S-Gogny [53]			Experiment [57–60]		
	B.E.	β_2	R_{ch}	B.E.	β_2	R_{ch}	B.E.	β_2	R_{ch}
^{20}Mg	133.79	0.0	3.119	136.22	0.0	3.01	134.47	0.440	
^{22}Mg	165.65	0.500	3.091	166.25	0.500	3.08	168.58	0.570	
^{24}Mg	193.73	0.500	3.072	193.25	0.537	3.10	198.26	0.609	3.057
^{26}Mg	211.75	−0.310	3.046	212.39	−0.309	3.05	216.68	0.489	3.034
	211.57	0.350	3.047						
^{28}Mg	228.08	0.335	3.071	228.49	0.0	3.02	231.63	0.503	
^{30}Mg	239.19	0.225	3.093	239.35	0.030	3.07	241.64	0.415	
	238.98	−0.200	3.092						
^{32}Mg	250.17	0.0	3.108	248.04	0.0	3.12	249.72	0.501	
^{34}Mg	254.16	0.350	3.180	252.43	0.393	3.20	256.71	0.553	
^{36}Mg	259.44	0.400	3.215	256.75	0.418	3.24	260.80	0.500	
^{38}Mg	261.34	0.450	3.257	258.71	0.418	3.26			
^{40}Mg	262.31	0.440	3.283	259.08	0.434	3.28			
^{42}Mg	261.08	0.375	3.293						

The stability of a nucleus is directly related to its binding energy and is also an important quantity to test a parameter set. The r.m.s. deviation of binding energies and charge radii is defined as

$$\begin{aligned}(\sigma_{\mathrm{rms}})_{\mathrm{BE}} &= \sqrt{\sum_{i=1}^{n}\frac{\left(E_i^{\mathrm{Exp}}-E_i^{\mathrm{Cal}}\right)^2}{n}}\,,\\ (\sigma_{\mathrm{rms}})_{R_{\mathrm{ch}}} &= \sqrt{\sum_{i=1}^{n}\frac{\left(R_i^{\mathrm{Exp}}-R_i^{\mathrm{Cal}}\right)^2}{n}}\,,\end{aligned} \qquad (20)$$

where n is the number of nuclei for which the r.m.s. deviation is calculated. The r.m.s. deviations of binding energy for these nuclei with DD-ME2 parameter set are 3.0006 MeV, 3.7455 MeV, 3.8978 MeV, and 3.2174 MeV for Mg, Si, S, and Ar isotopic chain, respectively. It can be observed from

TABLE II

The same as in Table I, but for $^{22-44}$Si isotopes.

Nuclei	DD-ME2			D1S-Gogny [53]			Experiment [57–60]		
	B.E.	β_2	R_{ch}	B.E.	β_2	R_{ch}	B.E.	β_2	R_{ch}
^{22}Si	132.82	0.0	3.283						
^{24}Si	167.80	−0.250	3.175	169.93	−0.229	3.13	172.01	0.245	
	167.61	0.300	3.208						
^{26}Si	200.83	0.400	3.187	202.31	−0.324	3.15	206.05	0.439	
	200.76	−0.300	3.153						
^{28}Si	231.62	−0.350	3.156	231.58	−0.370	3.17	236.54	0.407	3.122
^{30}Si	250.15	−0.250	3.151	251.64	0.0	3.10	255.62	0.311	3.134
	249.83	0.125	3.108						
^{32}Si	268.02	−0.200	3.165	267.57	0.010	3.15	271.41	0.228	
^{34}Si	283.83	0.0	3.174	281.14	0.0	3.20	283.43	0.183	
^{36}Si	290.41	0.150	3.207	289.19	0.0	3.21	292.01	0.265	
^{38}Si	297.67	0.300	3.265	296.12	0.285	3.27	299.93	0.255	
	297.09	−0.225	3.253						
^{40}Si	303.67	−0.300	3.300	302.18	−0.277	3.30	306.47	0.370	
	302.96	0.325	3.302						
^{42}Si	310.21	−0.350	3.340	308.15	−0.332	3.34			
^{44}Si	311.41	−0.300	3.346	309.29	−0.258	3.33			

Tables I–IV that there are only a few experimental data, for charge radii, available for Mg, Si, and S isotopes which would not be sufficient to calculate the r.m.s. deviation of charge radii ($(\sigma_{\mathrm{rms}})_{R_{\mathrm{ch}}}$). However, the value of $(\sigma_{\mathrm{rms}})_{R_{\mathrm{ch}}}$ for Ar isotopic chain is 0.0211 fm. The values of r.m.s. deviations of binding energy and charge radii are found to be comparable to the D1S-Gogny force.

In the PECs of these isotopic chains, a sudden shape transition is observed. Mainly, the Mg and Si isotopes show a sudden rise in deformation with the addition of neutrons. The origin of deformations is related to the evolution of the shell structure of single-particle orbitals. The nuclei with a magic number of nucleons (neutron or/and proton) form a closed shell which implies a spherical shape. However, this picture of spherical shape gets altered if the single-particle orbits are partially filled or by the excitation of nucleons to higher orbitals. To throw some light on the phenomena of nuclear deformation, we have shown, in Fig. 6, the neutron and proton single-particle energy levels for ^{20}Mg and ^{22}Mg. According to Jahn–Teller effect [66], the regions of low-level density around the Fermi surface favor the onset of deformation and are related to the ground-state minima in the potential energy curves. The upper two panels of Fig. 6 show single neu-

TABLE III

The same as in Table I, but for $^{26-56}$S isotopes.

Nuclei	DD-ME2			D1S-Gogny [53]			Experiment [57–60]		
	B.E.	β_2	R_{ch}	B.E.	β_2	R_{ch}	B.E.	β_2	R_{ch}
^{26}S	167.33	0.050	3.350	170.95	0.0	3.29			
^{28}S	205.31	0.350	3.296	207.11	0.127	3.25	209.41	0.265	
^{30}S	238.19	−0.250	3.265	240.15	0.030	3.21	243.68	0.339	
^{32}S	265.49	0.275	3.261	266.32	−0.030	3.23	271.78	0.301	3.261
^{34}S	287.06	−0.215	3.291	287.59	0.0	3.27	291.84	0.250	3.285
	286.23	0.125	3.275						
^{36}S	307.03	0.0	3.293	306.31	0.0	3.30	308.71	0.157	3.298
^{38}S	318.70	0.200	3.318	318.59	0.101	3.32	321.05	0.247	
	318.12	−0.100	3.311						
^{40}S	331.51	0.290	3.344	329.93	0.245	3.35	333.17	0.284	
^{42}S	341.60	0.275	3.359	339.79	0.301	3.39	344.12	0.300	
^{44}S	348.67	0.345	3.403	347.42	−0.242	3.39	351.82	0.258	
	347.83	−0.300	3.385						
^{46}S	353.24	0.275	3.411	352.91	−0.200	3.40			
	352.90	−0.225	3.405						
^{48}S	357.19	−0.225	3.431	356.93	0.0	3.39			
	357.06	0.200	3.419						
^{50}S	359.87	−0.225	3.468	358.11	0.0	3.42			
	359.66	0.160	3.437						
^{52}S	361.60	−0.160	3.484	357.07	0.0	3.46			
	361.44	0.125	3.472						
^{54}S	361.98	0.100	3.508						
^{56}S	362.24	0.0	3.542						

tron and proton levels corresponding to spherical configuration with $\beta_2 = 0$ for the ^{20}Mg nucleus. A large gap between the last occupied ($1p_{1/2}$) and the first unoccupied ($1d_{5/2}$) neutron orbits is observed. The ^{20}Mg nucleus has a neutron shell closure at $N = 8$. All neutron orbits below the Fermi level are occupied which leads to a spherical shape. The lower two panels of Fig. 6 present the neutron and proton single-particle energy levels in the ^{22}Mg nucleus as functions of the axial deformation parameter β_2. The solid curves present levels with positive parity and dashed curves denote levels with negative parity. Fermi levels are denoted by a thick black line. A large shell gap with $0.50 \leq \beta_2 \leq 0.55$ is observed around the Fermi level in the plots of single-particle energies for neutron and proton, respectively. The proton shell gap, however, is more pronounced than the neutron shell gap favoring the minima in the PEC of ^{22}Mg. This large proton shell gap is mainly formed by two levels split from the degenerate $1\pi d_{5/2}$ state favoring

TABLE IV

The same as in Table I, but for $^{28-58}$Ar isotopes.

Nuclei	DD-ME2			D1S-Gogny [53]			Experiment [57–60]		
	B.E.	β_2	$R_{\rm ch}$	B.E.	β_2	$R_{\rm ch}$	B.E.	β_2	$R_{\rm ch}$
^{28}Ar	162.44	0.125	3.506						
^{30}Ar	204.01	0.250	3.444						
	203.55	−0.200	3.430						
^{32}Ar	242.77	−0.240	3.381	244.13	−0.130	3.36	246.40	0.261	3.347
^{34}Ar	273.76	−0.225	3.382	275.35	0.020	3.35	278.72	0.235	3.365
	273.08	0.150	3.369						
^{36}Ar	302.69	−0.235	3.396	302.40	−0.180	3.37	306.72	0.257	3.391
^{38}Ar	326.52	0.0	3.387	326.64	0.0	3.39	327.34	0.159	3.403
^{40}Ar	341.92	−0.075	3.396	343.10	0.0	3.39	343.81	0.252	3.427
^{42}Ar	357.04	−0.175	3.414	357.77	0.053	3.41	359.34	0.273	3.435
	356.88	0.175	3.413						
^{44}Ar	370.93	−0.175	3.424	371.02	0.081	3.42	373.73	0.246	3.445
	370.64	0.175	3.423						
^{46}Ar	383.54	−0.180	3.434	382.66	0.0	3.43	386.92	0.196	3.438
^{48}Ar	391.57	−0.200	3.468	391.25	−0.190	3.48		0.228	
^{50}Ar	398.48	−0.230	3.504	398.30	0.0	3.47			
^{52}Ar	404.25	−0.260	3.547	402.08	0.0	3.50			
^{54}Ar	408.21	−0.175	3.556	404.33	0.0	3.54			
^{56}Ar	410.96	−0.125	3.582	405.62	0.0	3.57			
^{58}Ar	414.04	0.0	3.606	405.80	0.0	3.61			

the deformation, *i.e.*, the filling of [220]1/2 and [211]3/2 orbitals of $1d_{5/2}$ sub-shell, which are downsloping. However, the filling of [202]5/2 orbital of $1d_{5/2}$ sub-shell leads to a decrease in deformation due to its upsloping character. This decrease in deformation can be observed for the ^{26}Mg nucleus. Further, moving along the Mg isotopic chain, the deformation increases due to the mixing or special superpositions of single-particle states. The same can be said for Si isotopes. Thus, these ideas propose a simple comprehension of the several mechanisms leading to deformation in these isotopic chains.

In Fig. 7, the isotopic evolution of deformation parameter β_2 as a function of neutron number, N, is shown for all the isotopes of Mg, Si, S, and Ar. The comparison of the calculated values of the deformation parameter is done with the finite range droplet model (FRDM) and with available experimental data. In this figure, the progress of deformations with the neutron number, which is already seen in Figs. 2–5, is more apparent. In the Mg isotopic chain, all isotopes except ^{26}Mg have been shown to possess a prolate shape. The ^{20}Mg and ^{32}Mg nuclei have spherical shapes due

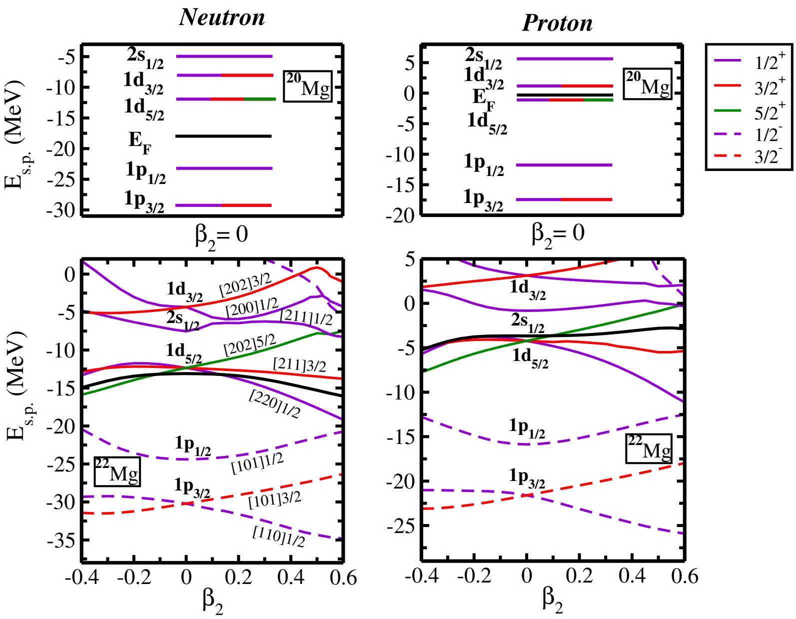

Fig. 6. Neutron and proton single-particle energy levels for ^{20}Mg and ^{22}Mg.

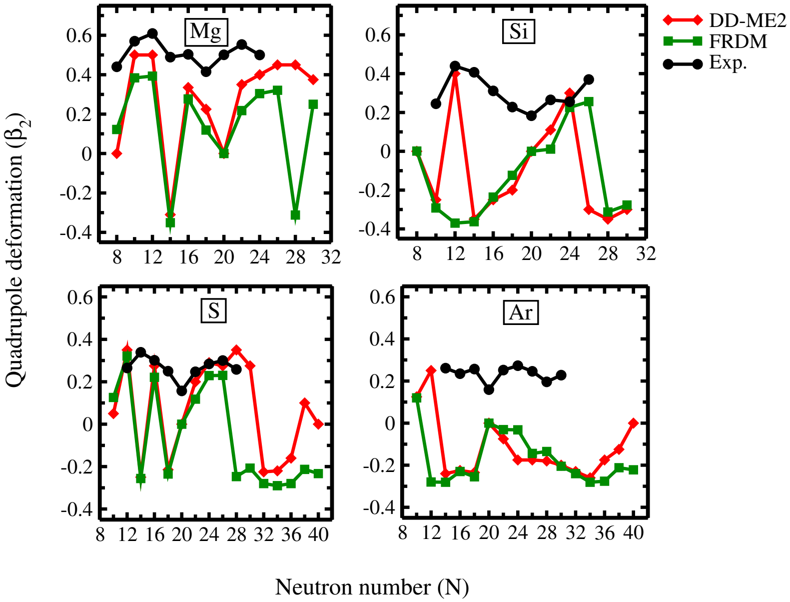

Fig. 7. The quadrupole deformation parameter (β_2) with respect to neutron number is plotted for Mg, Si, S and Ar isotopes. The comparison is made with FRDM data.

to the presence of $N = 8$ and $N = 20$ shell closures, respectively. Large prolate deformation is observed as one moves away from $N = 8$ shell closure. The nuclei above $N = 20$ shell closure also show a significant large deformation ($\beta_2 \sim 0.4$). It has been also noted that the Mg isotope with $N = 28$ shell closure takes a very large deformation ($\beta_2 \sim 0.45$), forced by a neutron mean-field, indicating the disappearance of shell closure and shell effect at $N = 28$. The Si isotopes are predicted to have large prolate as well as oblate deformations near the proton- and neutron-rich side. The disappearance of $N = 28$ shell closure is also visible in ^{42}Si, as it has a significant oblate deformation ($\beta_2 = -0.35$). A variety of shape transitions is seen throughout the S isotopic chain. A staggering type behavior of deformation parameter is observed up to $N = 20$ shell closure, indicating the softness of these isotopes. A large prolate deformation is observed on moving towards neutron-rich side which further becomes small on approaching neutron sub-shell closure at $N = 40$. Most of the Ar isotopes are seen to have an oblate ground state with a spherical shape at $N = 20$ shell closure and $N = 40$ sub-shell closure. The predictions of deformations in these isotopic chains are found to be in good agreement with that of the finite range droplet model and with experimental data.

In Fig. 8, we have presented the nuclei exhibiting the shape coexistence using the RHB model with DD-ME2 interaction. On the vertical axis, the energy difference between the prolate minima and oblate minima is shown. A positive value of ΔE implies that the prolate minima are more pronounced

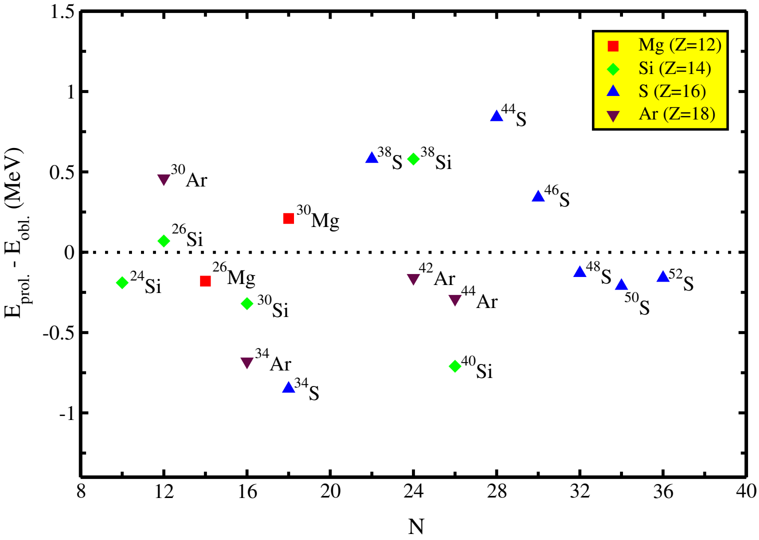

Fig. 8. The energy difference between prolate and oblate minima is plotted for shape coexisting candidates of Mg, Si, S and Ar isotopes.

than the oblate minima, while a negative value indicates that the oblate minima are deepest than the corresponding prolate minima. In the Mg chain presented here, the prolate shape is the lowest energy state. However, the ^{26}Mg and ^{30}Mg isotopes exhibit shape coexistence with $|\Delta E| = 0.2$ MeV. Many Si isotopes also show the shape coexistence phenomenon. The nuclei ^{24}Si, ^{26}Si, ^{30}Si, ^{38}Si, and ^{40}Si have almost degenerate prolate and oblate minima. Except for ^{26}Si and ^{38}Si, the other Si isotopes are oblate in the lowest energy state coexisting with a prolate minimum. Several isotopes of S that show the shape coexistence are: ^{34}S, ^{38}S, ^{44}S, ^{46}S, ^{48}S, ^{50}S, and ^{52}S. The positive value of ΔE for ^{38}S, ^{44}S, and ^{46}S indicates the prolate ground state for these nuclei. On the other hand, a negative value of ΔE for ^{34}S, ^{48}S, ^{50}S, and ^{52}S implies the oblate ground state. The value of ΔE is found to be very small for the ^{48}S, ^{50}S, and ^{52}S nuclei indicating the softness of these nuclei. Finally, the ^{30}Ar, ^{34}Ar, ^{42}Ar, and ^{44}Ar nuclei have also been found to be shape coexisting nuclei in the Ar isotopic chain. Except for ^{30}Ar, other nuclei have the oblate ground state coexisting with prolate minima a few keV above the lowest minima.

Figure 9 presents the isotope shifts for Mg, Si, S and Ar isotopic chains. The isotope shift for each isotopic chain is calculated relative to the mean-square nuclear charge radii of the reference nuclei with $N = 20$, given as

$$\delta \left\langle r_{\mathrm{ch}}^2 \right\rangle^{20,N} = \left\langle r_{\mathrm{ch}}^2 \right\rangle^{N} - \left\langle r_c^2 \right\rangle^{20} , \tag{21}$$

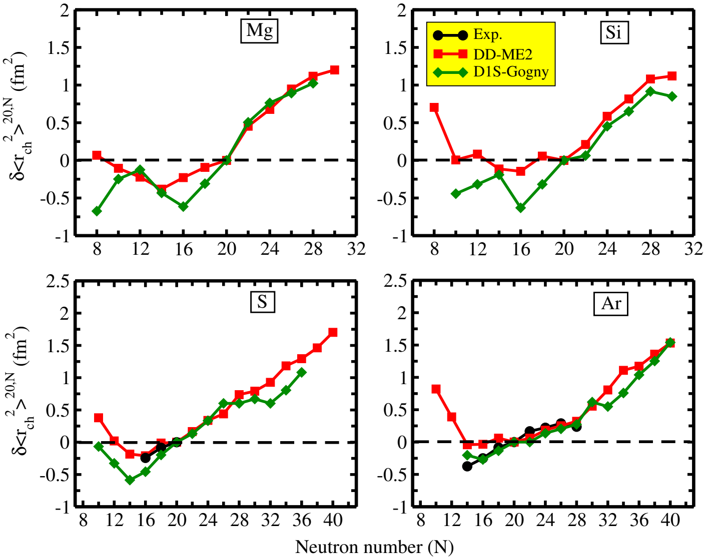

Fig. 9. Isotope shift for Mg, Si, S and Ar isotopes, calculated using the RHB model are compared with results of D1S-Gogny [53] and with experimental data [60].

where $\langle r^2_{\mathrm{ch}} \rangle$ is the mean-square charge radii of nuclei calculated from charge radius (R_{ch}) given in Tables I–IV. A parabola like behavior of isotope shifts is observed for all isotopic chains. The minima in the isotope shifts correspond to nuclei near the stability line. In Fig. 9, the ^{26}Mg, ^{30}Si, ^{32}S and ^{34}Ar nuclei show the minima in the isotope shifts. Moreover, these nuclei have smaller charge radii even as compared to the lighter neighbors. The isotope shift is observed to rise considerably towards the proton-rich side. This rise in isotope shift to the extreme left or towards the proton-rich side indicates the swelling of charge radius due to large proton skin. The trend of isotope shifts, in the present study, is compared with the results of HFB calculations using the D1S-Gogny force and with available experimental data.

3.2. Single-particle energy spectra of $N = 28$ isotones

The emergence of collectivity and shape coexistence phenomenon in the nuclei can be understood by the evolution of neutron and proton single-particle energy levels with quadrupole deformation and the occurrence of gaps around the Fermi level. The regions of low-level density favor the onset of deformation as explained in the Jahn–Teller effect [66]. The ground-state minima in the potential energy curve are associated with the effect of low-level density around the Fermi surface. The feature of deformation occurrence in the $N = 28$ isotones can be ascribed to the possibility of quadrupole correlations between the occupied and valence states.

Figures 10–13 present the neutron and proton single-particle energy levels for $N = 28$ isotones, calculated using the RHB model with DD-ME2 interaction. The increase in neutron $N = 28$ shell gap [55] and the near degeneracy of the $d_{3/2}$ and $s_{1/2}$ proton orbitals can be seen in these figures. In Fig. 10, the gap between occupied and unoccupied neutron levels is around $\beta_2 \approx -0.37$ favoring an oblate shape, while on the proton side, this gap is around $\beta_2 \approx 0.44$ which favors the onset of prolate deformation. The proton shell gap is more pronounced than the neutron gap leading to the prolate ground state of ^{40}Mg. The picture of magic nucleus [67] in ^{42}Si seems to be broken, in Fig. 11, as a large neutron and proton shell gaps are observed on the oblate side which results in the pronounced oblate minimum at $\beta_2 \approx -0.35$. In ^{44}S, the largest gap between neutron states is around $\beta_2 \approx -0.30$, that is, on the oblate side (left panel of Fig. 12). In the proton energy level spectra, the largest gap is found on the prolate side with deformation around $\beta_2 \approx 0.35$ (right panel of Fig. 12). The formation of the oblate neutron and prolate proton shell gaps is the origin of the coexistence of deformed shapes in ^{44}S (*cf.* Fig. 4). Finally, a large spherical gap is observed between occupied and unoccupied neutron levels, as shown in the left panel of Fig. 13. For proton states, the largest gap is observed around

$-0.23 \leq \beta_2 \leq -0.17$, that is, on the oblate side. The competition between the spherical shape favored by neutron states and the oblate shape favored by proton states leads to the shallow extended oblate minimum shown in Fig. 5.

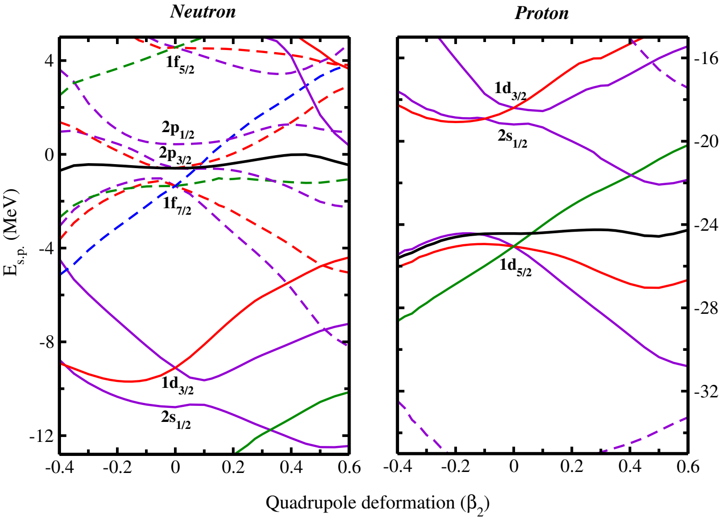

Fig. 10. Neutron and proton single-particle energy levels of ^{40}Mg as a function of quadrupole deformation parameter β_2. Solid curves present levels with positive parity, and dashed curves denote levels with negative parity. The thick black line denotes the corresponding Fermi energy levels.

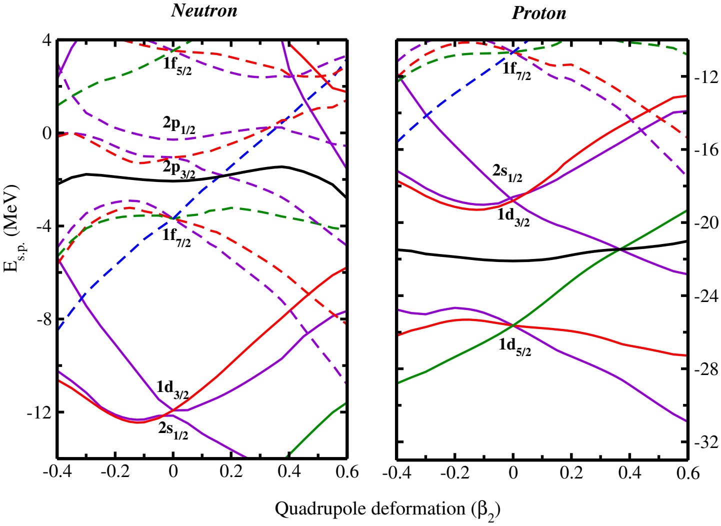

Fig. 11. The same as described in the caption of Fig. 10 but for the ^{42}Si nucleus.

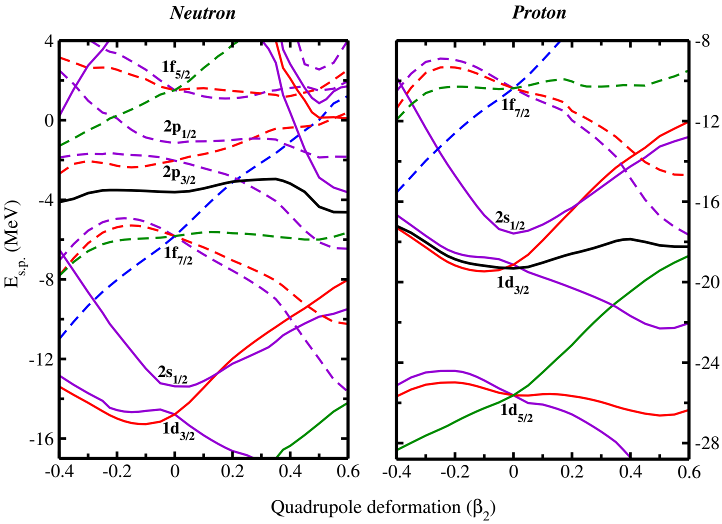

Fig. 12. The same as described in the caption of Fig. 10 but for the ^{44}S nucleus.

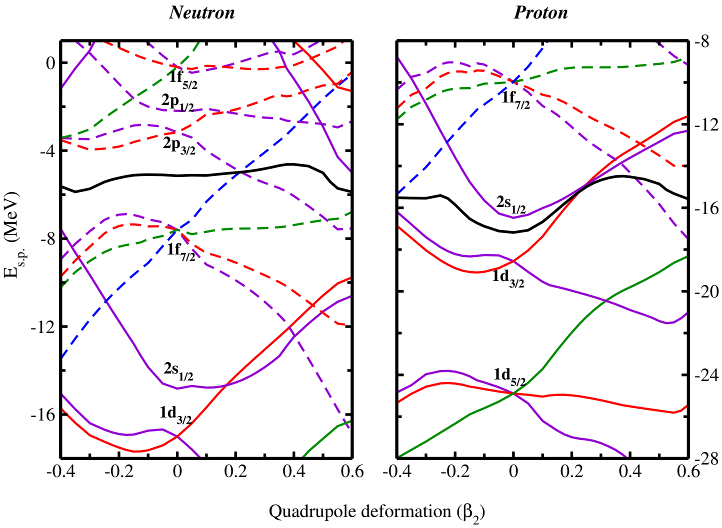

Fig. 13. The same as described in the caption of Fig. 10 but for the ^{46}Ar nucleus.

In Table V, the theoretically calculated neutron $N = 28$ spherical shell gaps, and the corresponding quadrupole deformation parameter for the minima of potential energy curves of ^{40}Mg, ^{42}Si, ^{44}S, ^{46}Ar, and ^{48}Ca are shown. A clear reduction of the spherical $N = 28$ shell gap is seen as one moves towards the proton-deficient side. It can be observed from Table V that the spherical gap between doubly magic ^{48}Ca and ^{46}Ar decreases from 4.8706 to 4.4351 MeV, which is in good agreement with experimental data [56, 68]. The theory and experiment, both points toward a strong disruption of the $N = 28$ spherical gaps as the isotones become more neutron-rich. It was shown in the RHB study of neutron-rich $N = 28$ isotones that the relativistic mean-field model reproduces the $N = 28$ shell gap due to the inclusion of the spin-orbit interaction and the isospin dependence of this term [22]. The removal of protons from a nucleus stimulates the energy change of the neutron levels due to the proton–neutron interaction. Experimentally, indirect evidence of the erosion of the gap has been obtained by following the evolution of excitation energies of the 2_1^+ state and the E2 transitions in $N = 28$ isotones and neighboring nuclei [55, 56]. The present findings of erosion of $N = 28$ shell gap in light nuclei are consistent with the results of RHB calculations with density-dependent point coupling (DD-PC1) interaction [12] and with other theoretical models.

TABLE V

Theoretically calculated neutron $N = 28$ spherical energy gaps, and the corresponding values of ground-state minima of the quadrupole binding energy maps of ^{40}Mg, ^{42}Si, ^{44}S, ^{46}Ar, and ^{48}Ca.

Nucleus	$\Delta^{\mathrm{sph}}_{N=28}$	β_2 [min]
^{40}Mg	1.8314	0.440
^{42}Si	2.7369	−0.350
^{44}S	3.7923	0.345
^{46}Ar	4.4351	−0.180
^{48}Ca	4.8706	0.0

4. Conclusion

In the present work, we have done self-consistent calculations using the relativistic Hartree–Bogoliubov (RHB) model with density-dependent meson exchange (DD-ME2) interaction. The pairing correlations have been taken into account by employing an interaction that is separable in momentum space. An extensive study of shape evolution and other ground-state properties has been done for Mg, Si, S, and Ar isotopic chains by taking axial symmetry into account. The study has covered complete isotopic chains from proton-rich side to neutron-rich side. The PECs gives a clear picture of shape evolution and shape transition for even–even isotopes of Mg, Si, S, and Ar. A sudden shape transition and large deformation are observed for these isotopic chains even near the nuclear drip lines. A positive value of chemical potential (λ_n) and negative value of two-neutron separation energy (S_{2n}) is predicted for ^{40}Mg which indicates a neutron drip line nucleus. Our calculations also indicate the drip line for ^{56}S due to a very small value of S_{2n}. In the present work, the proton drip line is observed for the ^{24}Si, ^{28}S, and for ^{32}Ar nucleus in these chains. Some isotopes of Mg, Si, S, and Ar isotopic chains are seen to exhibit well-deformed oblate–prolate shape coexistence with an energy difference of a few keV. A strong shell effect has been observed in these isotopic chains as the nuclei with the magic number of neutrons, $N = 8$ and 20, show a spherical shape. The ^{56}S and ^{58}Ar nuclei are observed to be spherical in their ground state indicating the presence of $N = 40$ sub-shell closure. However, the shell effects are washed out for the $N = 28$ magic number, as it shows different properties. It has been observed from the present study that the isotones of $N = 28$ magic number show a well-deformed minimum rather than spherical minima. The reduction of neutron shell gap between ^{48}Ca and ^{40}Mg favors the occurrence of particle–hole excitations between the occupied and valance orbits. An interesting case of ^{44}S nuclei is studied as this nucleus with $N = 28$ shows a strong prolate- and oblate-shape minima coexisting in the ground state. In conclusion, we can say that the deformation effect cannot be neglected in the structural characterization of light nuclei.

The authors are thankful to the Himachal Pradesh University for providing computational facilities. One of the authors, Pankaj Kumar, acknowledges the financial assistance Senior Research Fellowship provided by the Council of Scientific and Industrial Research (CSIR), New Delhi *vide* reference No. 09/237(0165)/2018-EMR-I. The authors would like to express deep and sincere gratitude to Prof. Peter Ring for a fruitful discussion.

REFERENCES

[1] L. Caceres *et al.*, «Shells and Shapes in the ^{44}S Nucleus», *Acta Phys. Pol. B* **42**, 533 (2011).

[2] C. Force *et al.*, «Prolate-Spherical Shape Coexistence at $N = 28$ in ^{44}S», *Phys. Rev. Lett.* **105**, 102501 (2010).

[3] G.A. Lalazissis, A.R. Farhan, M.M. Sharma, «Light nuclei near neutron and proton drip lines in relativistic mean-field theory», *Nucl. Phys. A* **628**, 221 (1998).

[4] A.A. Alzubadi, R.S. Obaid, «Study of the nuclear deformation of some even–even isotopes using Hartree—Fock—Bogoliubov method (effect of the collective motion)», *Indian J. Phys.* **93**, 75 (2019).

[5] N. Hinohara *et al.*, «Shape fluctuations in the ground and excited 0^+ states of ^{30,32,34}Mg», *Phys. Rev. C* **84**, 061302 (2011).

[6] K. Wimmer *et al.*, «Discovery of the Shape Coexisting 0^+ state in ^{32}Mg by a Two Neutron Transfer Reaction», *Phys. Rev. Lett.* **105**, 252501 (2010).

[7] A. Li, X.R. Zhou, H. Sagawa, «Tensor force and shape evolution of Si isotopes in the Skyrme–Hartree–Fock model», *Prog. Theor. Exp. Phys.* **2013**, 063D03 (2013).

[8] A.D. Davies *et al.*, «Probing Shell Structure and Shape Changes in Neutron-Rich Sulfur Isotopes through Transient-Field g-Factor Measurements on Fast Radioactive Beams of ^{38}S and ^{40}S», *Phys. Rev. Lett.* **96**, 112503 (2006).

[9] B. Bastin *et al.*, «Collapse of the $N = 28$ Shell Closure in ^{42}Si», *Phys. Rev. Lett.* **99**, 022503 (2007).

[10] S. Ebata, M. Kimura, «Low-lying 2^+ states generated by pn-quadrupole correlation and $N = 28$ shell quenching», *Phys. Rev. C* **91**, 014309 (2015).

[11] M. Zielińska *et al.*, «Shape of ^{44}Ar: Onset of deformation in neutron-rich nuclei near ^{48}Ca», *Phys. Rev. C* **80**, 014317 (2009).

[12] Z.P. Li *et al.*, «Energy density functional analysis of shape evolution in $N = 28$ isotones», *Phys. Rev. C* **84**, 054304 (2011).

[13] S. Gaurav, M. Kaushik, «$N = 28$ isotones: shape coexistence towards proton deficient side», *St. Petersburg State Polytechnical University Journal — Physics and Mathematics* **10**, 134 (2017).

[14] G.A. Lalazissis *et al.*, «Relativistic Hartree+Bogoliubov description of the deformed $N = 28$ region», *Phys. Rev. C* **60**, 014310 (1999).

[15] G.A. Lalazissis, D. Vretenar, P. Ring, «Relativistic Hartree–Bogoliubov description of sizes and shapes of $A = 20$ isobars», *Phys. Rev. C* **63**, 034305 (2001).

[16] J. Meng, S.-G. Zhou, I. Tanihata, «The relativistic continuum Hartree–Bogoliubov description of charge-changing cross section for C, N, O and F isotopes», *Phys. Lett. B* **532**, 209 (2002).

[17] J. Meng *et al.*, «Giant halo at the neutron drip line in Ca isotopes in relativistic continuum Hartree–Bogoliubov theory», *Phys. Rev. C* **65**, 041302 (2002).

[18] S. Thakur, S.K. Dhiman, «A study of shell structure in normal to exotic nuclides within relativistic Hartree–Bogoliubov approximation», *Mod. Phys. Lett. A* **34**, 1950014 (2019).

[19] V. Thakur, S.K. Dhiman, «A study of charge radii and neutron skin thickness near nuclear drip lines», *Nucl. Phys. A* **992**, 121623 (2019).

[20] V. Thakur *et al.*, «Microscopic study of the shell structure evolution in isotopes of light to middle mass range nuclides», *Nucl. Phys. A* **1002**, 121981 (2020).

[21] P. Kumar, S.K. Dhiman, «Microscopic study of shape evolution and ground-state properties in even–even Cd isotopes using covariant density functional theory», *Nucl. Phys. A* **1001**, 121935 (2020).

[22] P. Kumar *et al.*, «Nuclear shape evolution and shape coexistence in Zr and Mo isotopes», *Eur. Phys. J. A* **57**, 36 (2021).

[23] G.A. Lalazissis, T. Nikšić, D. Vretenar, P. Ring, «New relativistic mean-field interaction with density-dependent meson—nucleon couplings», *Phys. Rev. C* **71**, 024312 (2005).

[24] M. Bender, P.-H. Heenen, P.-G . Reinhard, «Self-consistent mean-field models for nuclear structure», *Rev. Mod. Phys.* **75**, 121 (2003).

[25] H. Kucharek, P. Ring, «Relativistic field theory of superfluidity in nuclei», *Zeit. Phys A* **339**, 23 (1991).

[26] P. Ring, «Relativistic mean field theory in finite nuclei», *Prog. Part. Nucl. Phys.* **37**, 193 (1996).

[27] B.D. Serot, J.D. Walecka, «Recent Progress in Quantum Hadrodynamics», *Int. J. Mod. Phys. E* **06**, 515 (1997).

[28] R.J. Furnstahl, B.D. Serot, «Quantum Hadrodynamics: Evolution and Revolution», *Comments Nucl. Part. Phys.* **2**, A23 (2000), `arXiv:nucl-th/0005072`.

[29] D. Vretenar, A.V. Afanasjev, G.A. Lalazissis, P. Ring, «Relativistic Hartree–Bogoliubov theory: static and dynamic aspects of exotic nuclear structure», *Phys. Rep.* **409**, 101 (2005).

[30] G.A. Lalazissis, «Relativistic Hartree–Bogoliubov theory and the isospin dependence of the effective nuclear force», *Prog. Part. Nucl. Phys.* **59**, 277 (2007).

[31] T. Nikšić, N. Paar, D. Vretenar, P. Ring, «DIRHB — A relativistic self-consistent mean-field framework for atomic nuclei», *Comput. Phys. Commun.* **185**, 1808 (2014).

[32] S. Typel, H.H. Wolter, «Relativistic mean field calculations with density-dependent meson–nucleon coupling», *Nucl. Phys. A* **656**, 331 (1999).

[33] F. Hofmann, C.M. Keil, H. Lenske, «Density dependent hadron field theory for asymmetric nuclear matter and exotic nuclei», *Phys. Rev. C* **64**, 034314 (2001).

[34] T. Nikšić, D. Vretenar, P. Finelli, P. Ring, «Relativistic Hartree–Bogoliubov model with density-dependent meson–nucleon couplings», *Phys. Rev. C* **66**, 024306 (2002).

[35] F. De Jong, H. Lenske, «Asymmetric nuclear matter in the relativistic Brueckner–Hartree–Fock approach», *Phys. Rev. C* **57**, 3099 (1998).

[36] Y. Tian, Z.-Y. Ma, P. Ring, «A finite range pairing force for density functional theory in superfluid nuclei», *Phys. Lett. B* **676**, 44 (2009).

[37] T. Nikšić *et al.*, «3D relativistic Hartree–Bogoliubov model with a separable pairing interaction: Triaxial ground-state shapes», *Phys. Rev. C* **81**, 054318 (2010).

[38] Y. Tian, Z.-Y. Ma, P. Ring, «Separable pairing force for relativistic quasiparticle random-phase approximation», *Phys. Rev. C* **79**, 064301 (2009).

[39] Y. Tian, Z.-Y. Ma, P. Ring, «Axially deformed relativistic Hartree Bogoliubov theory with a separable pairing force», *Phys. Rev. C* **80**, 024313 (2009).

[40] T. Nikšić, D. Vretenar, P. Ring, «Relativistic nuclear energy density functionals: Mean-field and beyond», *Prog. Part. Nucl. Phys.* **66**, 519 (2011).

[41] P.-G. Reinhard, «The relativistic mean-field description of nuclei and nuclear dynamics», *Rep. Prog. Phys.* **52**, 439 (1989).

[42] Zhao Peng-Wei, Sun Bao-Yuan, Meng Jie, «Deformation Effect on the Center-of-Mass Correction Energy in Nuclei Ranging from Oxygen to Calcium», *Chin. Phys. Lett.* **26**, 112102 (2009).

[43] J. Meng *et al.*, «Relativistic continuum Hartree Bogoliubov theory for ground-state properties of exotic nuclei», *Prog. Part. Nucl. Phys.* **57**, 470 (2006).

[44] J. Meng, P. Ring, «Relativistic Hartree–Bogoliubov Description of the Neutron Halo in ^{11}Li», *Phys. Rev. Lett.* **77**, 3963 (1996).

[45] J. Meng, P. Ring, «Giant Halo at the Neutron Drip Line», *Phys. Rev. Lett.* **80**, 460 (1998).

[46] J. Meng, S.-G. Zhou, «Halos in medium-heavy and heavy nuclei with covariant density functional theory in continuum», *J. Phys G: Nucl. Part. Phys.* **42**, 093101 (2015).

[47] S.-G. Zhou, J. Meng, P. Ring, «Spherical relativistic Hartree theory in a Woods–Saxon basis», *Phys. Rev. C* **68**, 034323 (2003).

[48] S.-G. Zhou *et al.*, «Neutron halo in deformed nuclei», *Phys. Rev. C* **82**, 011301 (2010).

[49] L. Li *et al.*, «Deformed relativistic Hartree–Bogoliubov theory in continuum», *Phys. Rev. C* **85**, 024312 (2012).

[50] K. Zhang *et al.*, «Deformed relativistic Hartree–Bogoliubov theory in continuum with a point-coupling functional: Examples of even–even Nd isotopes», *Phys. Rev. C* **102**, 024314 (2020).

[51] W. Koepf, P. Ring, «A relativistic description of rotating nuclei: The yrast line of ^{20}Ne», *Nucl. Phys. A* **493**, 61 (1989).

[52] J.M. Yao *et al.*, «Configuration mixing of angular-momentum-projected triaxial relativistic mean-field wave functions. II. Microscopic analysis of low-lying states in magnesium isotopes», *Phys. Rev. C* **83**, 014308 (2011).

[53] J.-P. Delaroche *et al.*, «Structure of even–even nuclei using a mapped collective Hamiltonian and the D1S Gogny interaction», *Phys. Rev. C* **81**, 014303 (2010).

[54] Ying Wang, Jian Li, Jing Bin Lu, Jiang Ming Yao, «A systematic study of even–even nuclei from Ne to Ca in covariant density functional theory with triaxiality», *Prog. Theor. Exp. Phys.* **2014**, 113D03 (2014).

[55] O. Sorlin, «The study of the $N = 28$ shell closure: a way to probe nuclear forces», *Nucl. Phys. A* **834**, 400c (2010).

[56] L. Gaudefroy *et al.*, «Reduction of the Spin-Orbit Splittings at the $N = 28$ Shell Closure», *Phys. Rev. Lett.* **97**, 092501 (2006).

[57] X.W. Xia *et al.*, «The limits of the nuclear landscape explored by the relativistic continuum Hartree–Bogoliubov theory», *Atom. Data Nucl. Data Tables* **121–122**, 1 (2018).

[58] Meng Wang *et al.*, «The AME2016 atomic mass evaluation (II). Tables, graphs and references», *Chin. Phys. C* **41**, 030003 (2017).

[59] S. Raman, C.W. Nestor Jr., P. Tikkanen, «Transition probability from the ground to the first-excited 2^+ state of even–even nuclides», *Atom. Data Nucl. Data Tables* **78**, 1 (2001).

[60] I. Angeli, K. Petrova Marinova, «Table of experimental nuclear ground-state charge radii: An update», *Atom. Data. Nucl. Data Tables* **99**, 69 (2013).

[61] J. Erler *et al.*, «The limits of the nuclear landscape», *Nature* **486**, 509 (2012).

[62] T. Baumann *et al.*, «Discovery of ^{40}Mg and ^{42}Al suggests neutron drip-line slant towards heavier isotopes», *Nature* **449**, 1022 (2007).

[63] N. Tsunoda *et al.*, «The impact of nuclear shape on the emergence of the neutron dripline», *Nature* **587**, 66 (2020).

[64] Q.Z. Chai, J.C. Pei, Na Fei, D.W. Guan, «Constraints on the neutron drip-line with the newly observed ^{39}Na», *Phys. Rev. C* **102**, 014312 (2020).

[65] K.Y. Zhang, D.Y. Wang, S.Q. Zhang, «Effects of pairing, continuum, and deformation on particles in the classically forbidden regions for Mg isotopes», *Phys. Rev. C* **100**, 034312 (2019).

[66] P.-G. Reinhard, E.W. Otten, «Transition to deformed shapes as a nuclear Jahn–Teller effect», *Nucl. Phys. A* **420**, 173 (1984).

[67] J. Fridmann *et al.*, «‘Magic’ nucleus ^{42}Si», *Nature* **435**, 922 (2005).

[68] L. Gaudefroy *et al.*, «Gaudefroy *et al.* Reply:», *Phys. Rev. Lett.* **99**, 099202 (2007).